Chinese Physics Letters

LETTER

# Anomalous Local Enhancement of Thermal Conductivity under Nanoscale Hotspot: Spatial Inhomogeneity and Phonon Nonequilibrium in Silicon

Cite as: Yuxin Luo *et al*. 2026 *Chin. Phys. Lett.* **43** 100703

## Recommended Articles

**Anomalous Thermal Transport in Silicon-Like Nanowires with One-Dimensional Correlated Disorder**
Wei Zhang, Shiyun Xiong, Yangyu Guo, Hongliang Yi, Masahiro Nomura, and Sebastian Volz
*Chin. Phys. Lett.* **42**, 120804 (2025)

**Using Targeted Phonon Excitation to Modulate Thermal Conductivity of Boron Nitride**
Dongkai Pan, Tianhao Li, Xiao Wan, Zhicheng Zong, Yangjun Qin, and Nuo Yang
*Chin. Phys. Lett.* **42**, 070801 (2025)

**Bonding Hierarchy and Phonon Coherence Enhanced Ultralow Lattice Thermal Conductivity and Excellent Thermoelectric Properties in $Cs_2TeI_6$**
Jing-Jing Zheng, Chao-jun Li, Rong-Rong Ma, Bao-Tian Wang, and Jiang-Jiang Ma
*Chin. Phys. Lett.* **42**, 080703 (2025)

**Theoretical Models on Interfacial Thermal Conductance of Nanoscale Solid Interfaces in Chips: A Mini Review**
Zhicheng Zong *et al*.
*Chin. Phys. Lett.* **41**, 106301 (2024)

**Anharmonic Phonon Dynamics and the Origin of Ultralow Lattice Thermal Conductivity in $CuBiI_4$: Implications for Thermoelectric Applications**
Feng Xiao, Qing-Yu Xie, Ru Yu, Junrong Zhang, and Bao-Tian Wang
*Chin. Phys. Lett.* **42**, 120702 (2025)

**Ultrahigh Lattice Thermal Conductivity in 2D Magnetic $VSi_2N_4$ Driven by Exceptional Stiffness**
Zhunyun Tang, Xiaoxia Wang, Shaogang Peng, Tao Ouyang, Jin Li, Chaoyu He, Mingxing Chen, Junjie He, and Chao Tang
*Chin. Phys. Lett.* **43**, 060801 (2026)

A series journal of Chinese Physical Society distributed by IOP Publishing

Chinese Physics Letters

*Chin. Phys. Lett.* **43** 100703 (2026)

LETTER

DOI: 10.1088/0256-307X/43/10/100703
CSTR: 32039.14.0256-307X.43.10.100703

# Anomalous Local Enhancement of Thermal Conductivity under Nanoscale Hotspot: Spatial Inhomogeneity and Phonon Nonequilibrium in Silicon

**Yuxin Luo(罗雨欣)[1], Shuai Wu(吴帅)[1], Dongdong Kang(康冬冬)[1,2,3], Xiaoxiang Yu(余晓翔)[1,2,3,*], and Jiayu Dai(戴佳钰)[1,2,3,*]**

[1]College of Science, National University of Defense Technology, Changsha 410073, China
[2]Hunan Key Laboratory of Extreme Matter and Applications, National University of Defense Technology, Changsha 410073, China
[3]Hunan Research Center of the Basic Discipline for Physical States, National University of Defense Technology, Changsha 410073, China

[*]Corresponding authors. Email: xxyu@nudt.edu.cn; jydai@nudt.edu.cn

**The miniaturization of electronic devices gives rise to localized heat accumulation and thus nanoscale hotspots, triggering degenerated heat dissipation. However, the phonon transport mechanism and quantification of inhomogeneous nonequilibrium thermal conductivity remain elusive. Here, through molecular dynamics simulations of silicon thin film under nanoscale hotspot, we reveal a dramatic spatial inhomogeneity of cross-plane thermal conductivity $\kappa_z$ under nanoscale hotspot excitation. Contrary to the conventional picture of phonon nonequilibrium simply suppressing heat transport, we find a non-monotonic spatial evolution: $\kappa_z$ drops by up to 68% immediately beneath the hotspot ($L_{hot}$ = 10.9 nm), but subsequently recovers to exceed the uniform-heating baseline by 12% at a distance of ~40 nm, producing a maximum $\kappa_z$ gradient of 3.2 W·m$^{-1}$·K$^{-1}$·nm$^{-1}$—2.3 times that of uniform heating. Spectral decomposition indicates that longitudinal acoustic (LA) phonons dominate the anomalous local thermal conductivity enhancement. Modal temperature calculations reveal that the spatial relaxation of hotspot-induced LA phonon nonequilibrium matches well with the transition of thermal conductivity from suppression to anomalous enhancement. The magnitude of the spatial inhomogeneity diminishes with rising temperature (from 3.05 W·m$^{-1}$·K$^{-1}$·nm$^{-1}$ at 300 K to 1.25 W·m$^{-1}$·K$^{-1}$·nm$^{-1}$ at 600 K) due to increased anharmonic scattering. These findings challenge the common assumption of spatially uniform thermal conductivity in hotspot systems and provide a quantitative, spectrally resolved benchmark for thermal management of nanoscale devices.**

With the increasing device density and progressive device miniaturization, thermal management issue has become a critical bottleneck restricting device performance [1–4]. As channel dimensions shrink to the nanoscale, generated Joule heat is localized in nanoscale region and accumulates rapidly [5,6], causing a sharp rise in local temperature and the formation of nanoscale "hotspot" [7–11], thus accurate measurement [12] or prediction [13,14] of thermal conductivity thus becomes even more crucial. Phonons, as the dominant heat carriers in semiconductor materials, govern the heat dissipation in transistors [15–18]. Since the size of nanoscale "hotspot" is comparable to the mean free path (MFP) and wavelength of phonons, heat conduction in such system is expected to exhibit quasi-ballistic behavior, making diffusive Fourier's law invalid [19–27]. Quantifying the nanoscale hotspot-induced non-Fourier heat conduction is essential to precisely evaluate and optimize the thermal management in nanodevices [28].

In recent years, numerous studies have thoroughly revealed the non-Fourier heat conduction phenomena; however, these studies mainly focused on the effects of system size [15,16,29–33], and reported the thermal transport is dominated by low-frequency phonons [34,35]. Targeting the nanoscale hotspot, relevant experimental studies have reported the negative heater size dependence of effective thermal conductivity by means of time-domain thermo-reflectance [26,27,36] and transient thermal grating [37], based on the assumption of spatially homogeneous thermal conductivity throughout the system [23–27,32,37–39]. Through tip-enhanced Raman measurement, the nonequilibrium phonon modes are observed around the sub-10 nm hotspot [19,21–23,40], and through extending near-field thermal radiation to the ultrafast time domain, the nonlocal and nonequilibrium phonon transport effects at the nanoscale are investigated [41], the nonequilibrium state of phonons significantly affects the thermal conductivity of materials [42]. From the center to outer region, the phonon nonequilibrium gradually vanishes and would induce spatially inhomogeneous thermal conductivity, which has not been clarified. Furthermore, quantitative spatial distribution of $\kappa(z)$ under hotspot and its spectral origin remain unclear.

In this work, through molecular dynamics (MD) simulations [43–45], we reported the dramatic inhomogeneity and nonmonotonic trend of cross-plane thermal conductivity $\kappa_z$ in silicon thin films with nanoscale hotspot. Compared with uniform heating, we found a lower $\kappa_z$ near the hotspot but a maximum $\kappa_z$ locating around 40 nm far from the hotspot, especially, surpassing uniform-heating baseline. We attributed the anomalously spatial variation of $\kappa_z$ to the thermalization of nonequilibrium phonons. Through frequency-domain spectral analysis, nanoscale heat sources significantly suppress the heat transport of low-frequency phonons, elucidating the position and heater size dependence of $\kappa_z$. This work provides fundamental insights into nonequilibrium phonon transport and quantitative guidance for the thermal management of nanodevices.

All MD simulations were performed using the GPUMD code [46]. The nonequilibrium molecular dynamical (NEMD) method [47] is adopted to calculate the $\kappa_z$ of silicon thin films with nanoscale hotspot. Unlike conventional phonon Boltzmann transport equation [19] and Monte Carlo methods [9] limited by equilibrium phonon parameters and the relaxation time approximation, MD can fully capture strong nonequilibrium phonon behaviors and inhomogeneous thermal transport near nanoscale hotspots, rendering it ideal for thermal transport studies under strongly nonequilibrium and extreme conditions [48–52].

In conventional NEMD simulations, two uniform thermostats are placed at the two ends of the system to establish a linearly distributed temperature gradient and a uniform heat flux throughout the system

Received 27 June 2026; accepted 2 September 2026; published 28 October 2026
© 2026 Chinese Physical Society and IOP Publishing Ltd. All rights, including for text and data mining, AI training, and similar technologies, are reserved.

Check for updates

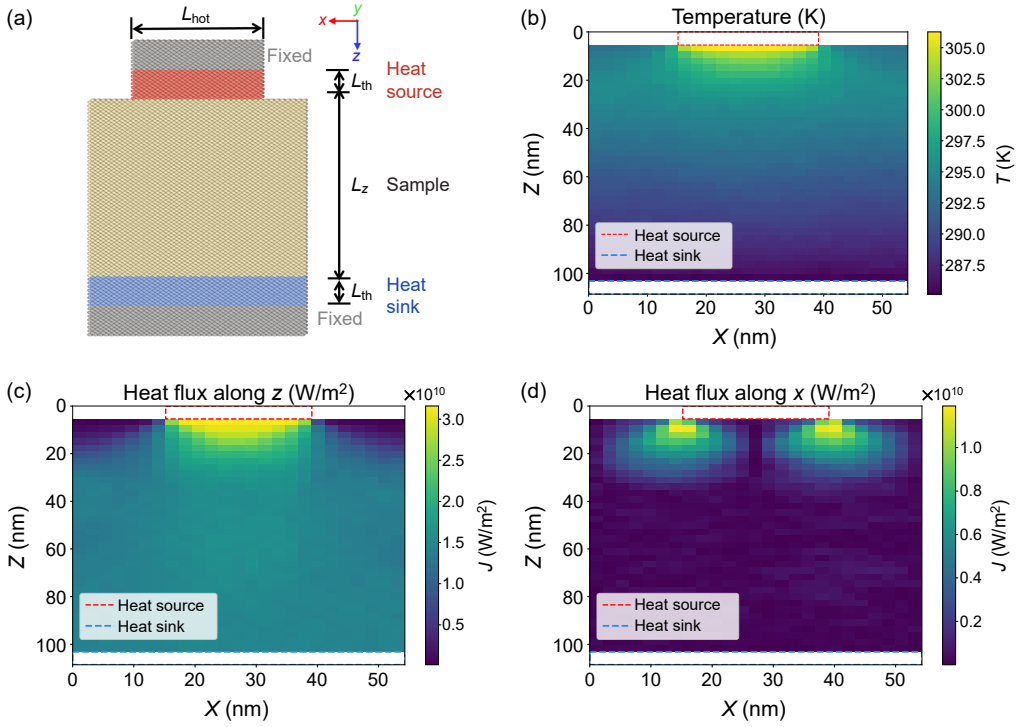


**Fig. 1.** Schematic of the NEMD simulation system and spatial inhomogeneity of thermal transport with a heat source size of 23.9 nm. (a) The heat source is configured as a protruding segment. Spatial (b) temperature and (c) and (d) heat flux distributions show 'lightbulb' shape.

[31,47,53]. In our simulations, as illustrated in Fig. 1(a), the heat source is configured as a localized high-temperature region of specific size ($L_{hot}$), implemented as a protruding segment in the *xy* plane of thin film, mimicking the nanoscale hotspot. Herein, the effect of $L_{hot}$ along the *x*-direction is investigated. Since periodic boundary conditions are applied in the *x*- and *y*-directions, heat transfer occurred only along the *x*- and *z*-directions. The interatomic interactions were described using the Tersoff potential, which has been widely and accurately applied in the investigation of thermal transport properties of silicon [54–56]. More simulation details are given in the Appendix C of the Supplementary Materials (SM).

Nanoscale hotspot causes bidirectionality and spatial inhomogeneity of thermal transport, as depicted in Figs. 1(b)–1(d). The system is divided into two-dimensional grids to characterize the spatial evolution of temperature and heat flux $J$ along the in-plane *x*- and cross-plane *z*-directions. In the region near the hotspot ($Z < 40$ nm), there exists both cross-plane and in-plane temperature gradients and, accordingly, in-plane heat flux comparable to that in cross-plane direction. The distributions of temperature and $J_z$ both show 'single-lightbulb' shape while the $J_x$ distribution shows 'double-lightbulb' shape. In the region far from the hotspot ($Z > 40$ nm), the cross-plane conduction dominates thermal transport overwhelmingly.

For the cross-plane heat transport, in comparison with uniform heating, nanoscale hotspot leads to nonlinearity. Beneath the hotspot, we focused on the middle region with width equal to the hotspot and divide this region into many slabs and calculated the average temperature, $J_z$ (heat flux along the *z*-direction), and effective $\kappa_z$ in each slab. For uniform heating, temperature distribution is linear and $J_z$ is constant along the *z*-direction, as shown by the black lines in Figs. 2(a) and 2(b). The temperature jump of the heat source and system increases as the size of the hotspot decreases, indicating a larger discrepancy in phonon distribution between the heat source and the system, and a greater degree of nonequilibrium. Nanoscale hotspot induces nonlinear distribution characteristics of temperature and heat flux in the system, with the degree of nonlinearity gradually decreasing along the *z*-direction. Meanwhile, as the heat source size decreases, the nonlinear evolution trend is significantly enhanced. More details regarding the calculations are provided in the Appendix C of SM.

According to the temperature gradient and $J_z$, we employed a sliding window method to calculate the effective thermal conductivity $\kappa_z$,

$$\kappa_z = -\frac{J_{avg}}{\Delta T/\Delta l};$$

the window size is set to 5 groups of temperature and $J_z$ data, with a step size of 2. Here, $J_{avg}$ is mean heat flux over the window, $\Delta T$ is temperature drop across the window, $\Delta l$ is the heat propagation distance associated with each statistical window. The local effective thermal conductivity calculated from Fourier's law here is not an intrinsic material property. Instead, it serves as an apparent transport coefficient to quantify nonequilibrium heat transport under nanoscale-hotspot heating.

The distribution of the $\kappa_z$ exhibit a pronounced spatial inhomogeneity, as shown in Fig. 2(c). For uniform heating, the $\kappa_z$ is 118.6 $W{\cdot}m^{-1}{\cdot}K^{-1}$ in the middle region, similar to previous simulations [31]. Nanoscale hotspot induces remarkable decreases in $\kappa_z$ in the region adjacent to the nanoscale heat source while negligible influences on $\kappa_z$ near the heat sink. Especially, while the $L_{hot}$ is 10.9 nm, the minimum $\kappa_z$ reaches as low as 24.0 $W{\cdot}m^{-1}{\cdot}K^{-1}$, representing a maximum reduction of 68% compared with that under uniform heating. The inhibitory effect on $\kappa_z$ increases significantly with the decrease in $L_{hot}$.

As the thermal transport proceeds along the *z*-direction, the $\kappa_z$ gradually increases, showing a large $\kappa_z$ gradient of 3.2 $W{\cdot}m^{-1}{\cdot}K^{-1}{\cdot}nm^{-1}$ before $Z = 40$ nm, 2.3 times of that under uniform heating (1.4 $W{\cdot}m^{-1}{\cdot}K^{-1}{\cdot}nm^{-1}$). Interestingly, nanoscale hotspot causes anomalous local enhancements of $\kappa_z$ around $Z = 40$ nm. Especially, when the heat source size is 10.9 nm, the maximum $\kappa_z$ appears at 43.44 nm away from the heat source, exceeds uniform heating by 12%, and reaches 131.6 $W{\cdot}m^{-1}{\cdot}K^{-1}$. Notably, the smaller the $L_{hot}$, the larger the maximum $\kappa_z$. After $Z = 50$ nm, the spatial distributions of $\kappa_z$ for different $L_{hot}$ are close to that under uniform heating.

The phonon nonequilibrium effect exhibits significant anomalous spatial distribution differences during the propagation from the nanoscale heat source. To clarify the correlation between phonon nonequilibrium transport and heterogeneous $\kappa_z$ distribution, seven representative positions $z_i$ are selected, as illustrated in Fig. 2(c). By spectral decomposition of heat flux [57], we calculated the spectral ther-

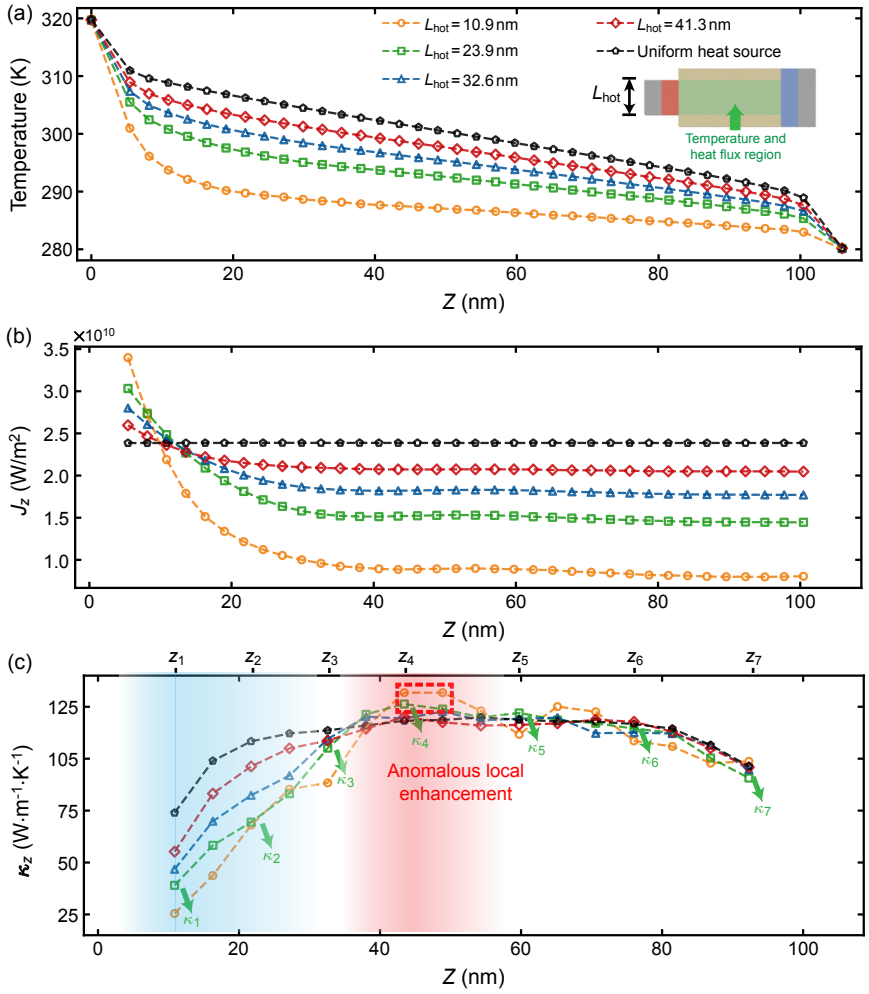


**Fig. 2.** Nonlinear cross-plane thermal transport induced by nanoscale hotspot. (a) Temperature, (b) heat flux $J_z$, and (c) effective $\kappa_z$ along the $z$-direction. The black dotted line denotes the reference case of uniform heating, while the other solid lines correspond to the cases of different heat source sizes, respectively.

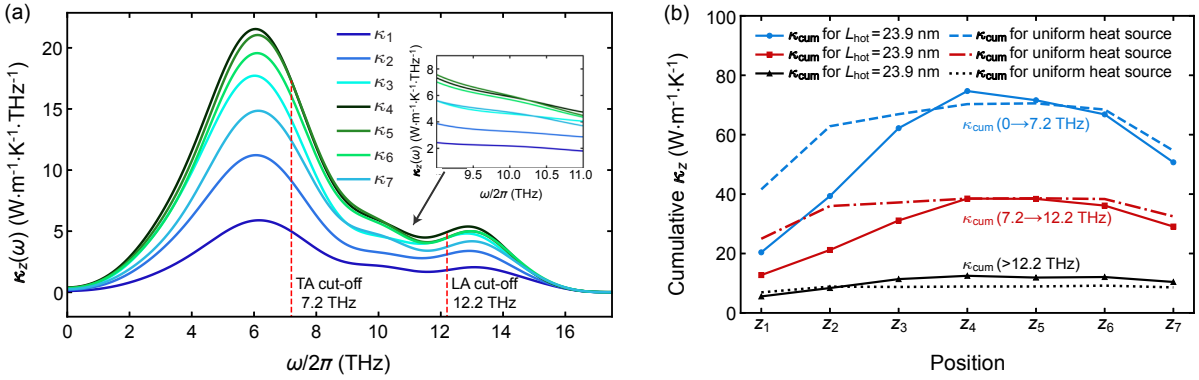


**Fig. 3.** Phonon mechanism of spatial heterogeneity of $\kappa_z$ with $L_{hot}$ = 23.9 nm. (a) $\kappa_z(\omega)$ at different characteristic positions $z_i$ shows a significant spatial inhomogeneous distribution. (b) Spectral cumulative $\kappa_z$ in different frequency regimes exhibit non-monotonic spatial variation at different characteristic positions $z_i$. The blue, red, and black lines represent the contributions of low-frequency (lower than 7.2 THz), mid-frequency (7.2 THz to 12.2 THz), and high-frequency (higher than 12.2 THz) phonons to $\kappa_z$. For uniform heating, the cumulative $\kappa_z$ are shown as dashed lines.

mal conductivity $\kappa_z(\omega)$ for a $L_{hot}$ of 23.9 nm, and the results are shown in Fig. 3.

As shown in Fig. 3(a), under the influence of nanoscale heat sources, the $\kappa_z(\omega)$ exhibits a spatially uneven distribution trend similar to that of $\kappa_z$ as shown in Fig. 2(c). From $z_4$ to $z_7$, $\kappa_z(\omega)$ moderately decays throughout the frequency range, due to phonon nonequilibrium phenomena near the uniform heat thermostat [58]. From $z_4$ to $z_1$, the attenuation of $\kappa_z(\omega)$ near the nanoscale hotspot is further strengthened. As $z_1$ is closest to the heat source, the entire frequency domain is strongly suppressed due to significant phonon nonequilibrium near the nanoscale hotspot. The position $z_4$ shows the highest value in the entire frequency domain, with its peak (21.94 W·m$^{-1}$·K$^{-1}$·THz$^{-1}$) near 6 THz being the most prominent.

By calculating the phonon spectrum, we obtained the highest cutoff frequency of 7.2 THz for the transverse acoustic (TA) phonon and the highest cutoff frequency of 12.2 THz for the longitudinal acoustic (LA) phonon at the first Brillouin zone edge. Detailed calculation results of this part are provided in the SM. To clarify this evolutionary

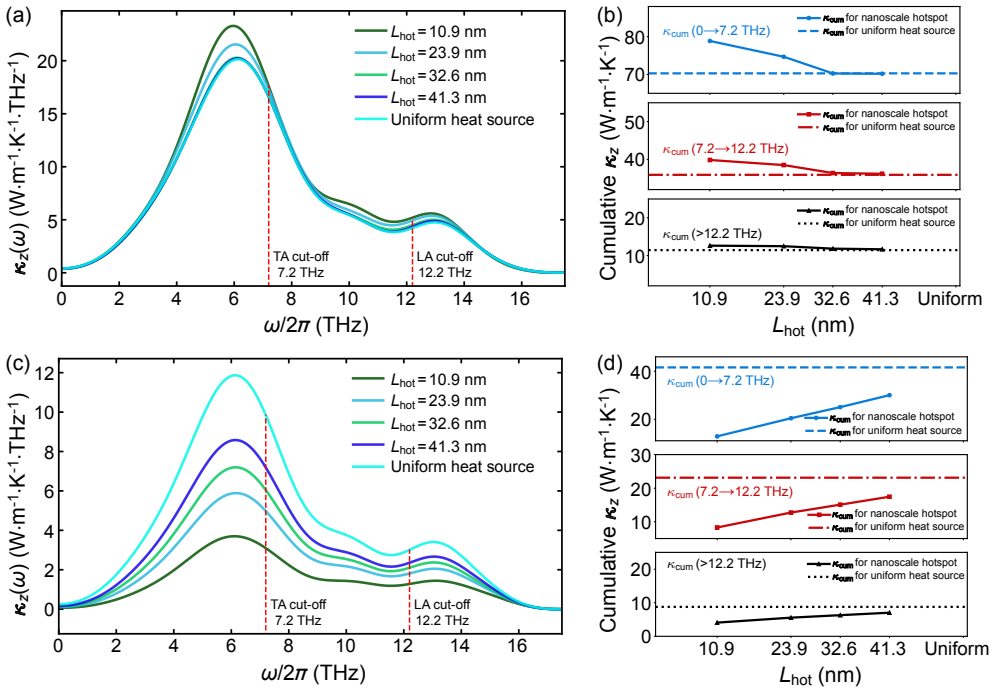


**Fig. 4.** The nanoscale hotspot size dependence of spectral and cumulative $\kappa_z$ at the positions with anomalous local $\kappa_z$ enhancement ($z_4$) and near the heat source ($z_1$). (a) and (b) $\kappa_z(\omega)$ and cumulative $\kappa_z$ at position $z_4$ firstly increase and then converges with increasing $L_{hot}$. (c) and (d) $\kappa_z(\omega)$ and cumulative $\kappa_z$ at position $z_1$ show monotonic increase. The blue, red, and black lines represent the contributions of low-frequency (lower than 7.2 THz), mid-frequency (7.2 THz to 12.2 THz), and high-frequency (higher than 12.2 THz) phonons to $\kappa_z$. For uniform heating, the results are shown as dashed lines.

mechanism, we calculated the cumulative $\kappa_z$ and compared the cases with $L_{hot}$ = 23.9 nm and uniform heating, as shown in Fig. 3(b). By comparing the results of $L_{hot}$ = 23.9 nm and uniform heating, we found that at $z_1$, the cumulative $\kappa_z$ of phonons in all three frequency bands is suppressed in the former case, while at $z_4$, the cumulative $\kappa_z$ of low- and medium-frequency phonons in the former case is higher than that in the latter case, indicating that the spatial evolution of the phonon contribution to $\kappa_z$ is non-monotonic.

When $L_{hot}$ = 23.9 nm, for any position of $\kappa_z(\omega)$, low-frequency phonons below 7.2 THz contribute most of the $\kappa_z$, which occupies 54% of total cumulative $\kappa_z$ for $\kappa_1$ (20.39 W·m$^{-1}$·K$^{-1}$) and 61% for $\kappa_4$ (74.69 W·m$^{-1}$·K$^{-1}$). We can observe that the change in the low-frequency phonon cumulative $\kappa_z$ from position $\kappa_1$ to $\kappa_4$ is significantly larger than that from $\kappa_4$ to $\kappa_7$. This indicates that the degree of phonon nonequilibrium near the nanoscale heat source is higher than that in the uniform heat sink region induced by ballistic phonon transport. Possessing long MFPs, these long-wave acoustic phonons experience strong ballistic nonequilibrium effects near the nanoscale hotspot, which significantly suppresses their contribution to $\kappa_z$.

When $L_{hot}$ = 23.9 nm, for frequencies above 12.2 THz, which are primarily attributed to optical phonons, the scattering tends to be strong and the lifetimes relatively short, which can lead to a relatively quick establishment of local thermal equilibrium. It can be seen from Fig. 3(b) that as the heat propagation distance increases, the phonon contribution becomes less sensitive to the propagation distance and tends to converge. This indicates that the nanoscale heat source has a weak effect on high-frequency phonons. And for mid-frequency phonons in the range of 7.2–12.2 THz, which are mainly LA modes, the phonon contribution to $\kappa_z$ near the heat source ($z_1$) is suppressed, with a value of 11.02 W·m$^{-1}$·K$^{-1}$. In contrast, in the intermediate region ($\kappa_4$), phonons in this frequency band still contribute significantly to $\kappa_z$, reaching 33.36 W·m$^{-1}$·K$^{-1}$. Overall, however, the cumulative $\kappa_z$ of mid-frequency phonons is lower than that of low-frequency phonons and is less affected by the nanoscale heat source.

The trends discussed above are also observed for other $L_{hot}$ cases, and we further find that as $L_{hot}$ approaches the uniform heating condition, the spatial distribution of cumulative $\kappa_z$ becomes increasingly uniform, indicating that the nonequilibrium effects induced by the nanoscale hotspot gradually decrease. Results for other $L_{hot}$ cases as well as those for uniform heating are presented in the Appendix D of SM.

We further calculated the $\kappa_z(\omega)$ and cumulative $\kappa_z$ under different $L_{hot}$, focusing mainly on the positions with anomalous local $\kappa_z$ enhancement ($z_4$) and near the heat source ($z_1$), as shown in Fig. 4. For position $z_4$, as $L_{hot}$ continues to increase and $\kappa_z(\omega)$ gradually approaches the uniform heat source (54.3 nm), $\kappa_z(\omega)$ at this location shows a stepwise change. When $L_{hot}$ = 10.9 nm and 23.9 nm, $\kappa_z(\omega)$ is higher than the uniform heating result; As the $L_{hot}$ continues to increase to 32.6 nm and 41.3 nm, their values gradually approach the $\kappa_z$ under uniform heating conditions, as shown in Fig. 4(a). The cumulative $\kappa_z$ of different sizes behaves similarly. As shown in Fig. 4(b), in the low-frequency range (less than 7.2 THz), the cumulative $\kappa_z$ is 76.53, 75.36, 72.57, and 70.41 W·m$^{-1}$·K$^{-1}$ respectively (72.36 W·m$^{-1}$·K$^{-1}$ for uniform heating). For the mid frequency range phonons (mainly LA) from 7.2 THz to 12.2 THz, the cumulative $\kappa_z$ remains relatively large, with values of 32.93, 33.19, 32.37, and 31.47 W·m$^{-1}$·K$^{-1}$ respectively (32.04 W·m$^{-1}$·K$^{-1}$ for uniform heating).

As mentioned earlier, a strong phonon nonequilibrium phenomenon appeared in the region near the nanoscale hotspot, which further intensified with the decrease of $L_{hot}$. As illustrated in Fig. 4(c), the $\kappa_z(\omega)$ of all nanoscale heat sources is lower than that of uniform heating, and the maximum decrease in peak value near 6 THz is 45.8% (occurring at $L_{hot}$ =10.9 nm). Meanwhile, figure 4(d) shows that the cumulative $\kappa_z$ of phonons in the three frequency domains in this region is strongly suppressed compared to uniform heating. In conclusion, nanoscale hotspot size governs phonon nonequilibrium thermal transport. Near the heat source, phonon conduction is universally suppressed. In the enhanced $\kappa_z$ region, thermal properties gradually shift from exceeding to falling below uniform heating results, which is dominated by low-and mid-frequency phonons.

We decomposed the spectral thermal conductivity into L and T mode contributions at various nanoscale hotspot sizes and spatial positions along the heat propagation direction. As the hotspot size increases, the spatial variation of both L- and T-mode spectral thermal

conductivity diminishes. Furthermore, the spatial variation of the T-mode contribution is substantially greater than that of the L-mode. Additional details are provided in the Appendix D of SM. Based on the cutoff frequencies of the LA and TA branches obtained from the phonon dispersion results, we further acquired the thermal conductivity contribution of acoustic phonons, as illustrated in Fig. 5. It is found that phonons belonging to the LA branch play a more crucial role in thermal conduction over the entire spatial region of the material.

To better interpret and rationalize the anomalous enhancement in thermal conductivity, we calculated mode-resolved phonon temperatures and explored the spatial evolution of phonon nonequilibrium within the system. The phonon modal temperatures were extracted from our NEMD simulations via the spectral phonon temperature (SPT) method proposed by Feng *et al*. [59], which map the real-space atomic vibration in NEMD to the reciprocal-space phonon properties [58].

We compared and analyzed the SPT of acoustic phonons, with particular focus on LA-branch phonons, and examined the SPT at different *k*-points, as shown in Fig. 6. We found that the nonequilibrium degree of modal temperatures induced by hotspot heating is markedly higher for the LA, TA1, and TA2 phonon branches than that under uniform heating. For the LA branch, which dominates thermal transport, the modal temperature disparity among different *k*-points under uniform heating is relatively slight. In contrast, under hotspot heating, the temperature discrepancies between distinct phonon modes decrease evidently as heat propagates, approaching equilibrium at a distance of 43 nm, which coincides closely with the location where anomalous enhancement of thermal conductivity occurs. The computational details of SPT and the results of other phonon branches are available in the Appendix E of SM.

To elucidate the evolution of phonon nonequilibrium behavior induced by nanoscale hotspot at high temperatures, we compared the

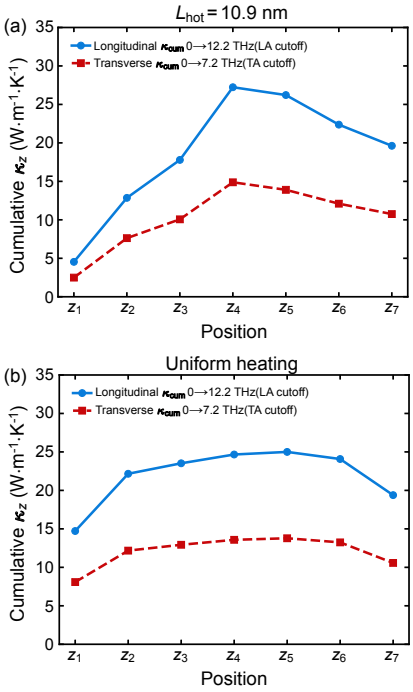


**Fig. 5.** The spatial thermal conductivity contribution of acoustic phonons under hotspot and uniform heating. Cumulative $\kappa_z$ of acoustic phonons at different characteristic positions $z_i$ shows a significant spatial inhomogeneous distribution, LA branch plays a more crucial role in thermal conduction over the entire spatial region of the material. (a) $L_{hot}$ = 10.9 nm, (b) uniform heating. The blue dotted line denotes the thermal conductivity contribution of LA-branch phonons, while the red dashed line represents that of TA-branch phonons.

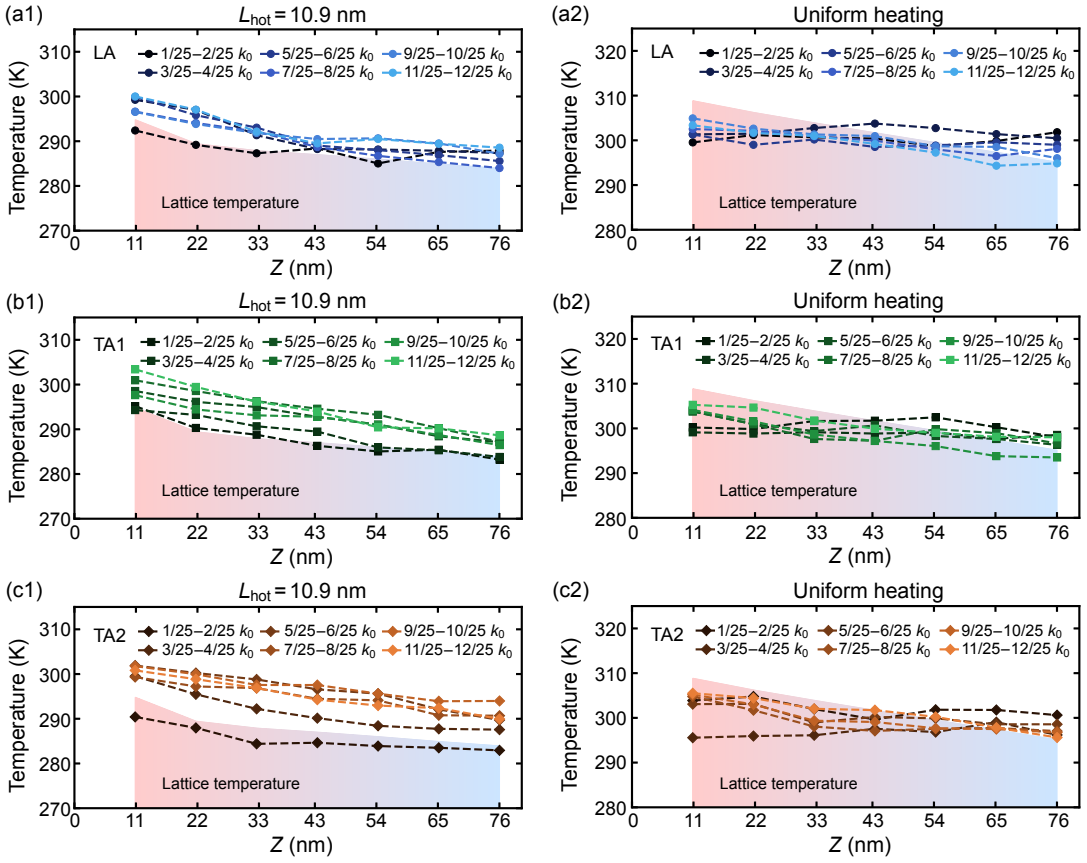


**Fig. 6.** The spatial SPT of acoustic phonons at different *k*-points under hotspot and uniform heating, (a1), (b1), and (c1) show the results for the LA, TA1, and TA2 phonon branches under hotspot heating ($L_{hot}$ = 10.9 nm), respectively; while (a2), (b2), and (c2) correspond to those under uniform heating. We display the mode–temperature results of phonon modes associated with wavevectors in the first Brillouin zone, and average the data for each pair of neighboring wavevectors.

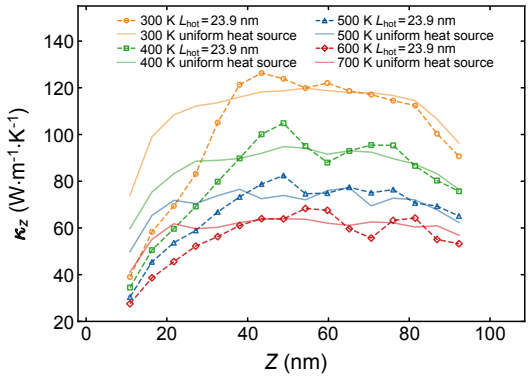


**Fig. 7.** Nonlinear cross-plane thermal transport induced by nanoscale hotspot at elevated temperatures. The simulation temperatures 300 K, 400 K, 500 K, and 600 K are represented by orange, green, blue, and red, respectively. As the temperature increases, the inhibitory effect of nanoscale hotspot on heat transport in its surrounding regions and the anomalous enhancement of $\kappa_z$ both gradually decrease.

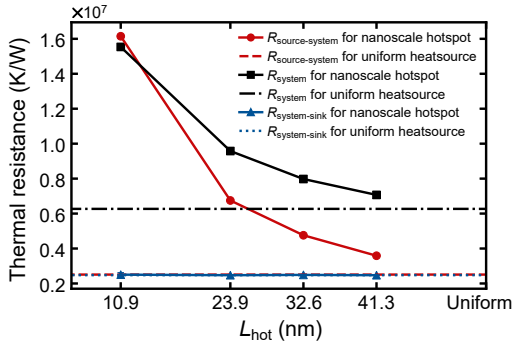


**Fig. 8.** Thermal resistances under different heating sizes. The system thermal resistance, heat source-system thermal resistance, and heat sink-system thermal resistance are depicted as black, red, and blue lines, respectively. For uniform heating, the results are shown as dashed lines. As $L_{hot}$ increases, the system thermal resistance and heat source-system thermal resistance decrease and approach the values under uniform heating.

difference in $\kappa_z$ between $L_{hot}$ = 23.9 nm and uniform heating at 300 K, 400 K, 500 K, and 600 K, as shown in Fig. 7. The system temperature distributions and heat fluxes under different heat bath temperatures are provided in the SM. As the temperature increases, the inhibitory effect of nanoscale hotspot on heat transport in its surrounding regions and the anomalous enhancement of $\kappa_z$ both gradually decrease. The magnitude of the spatial inhomogeneity diminishes with rising temperature, from 3.05 W·m$^{-1}$·K$^{-1}$·nm$^{-1}$ at 300 K to 1.25 W·m$^{-1}$·K$^{-1}$·nm$^{-1}$ at 600 K. At position $z_1$, the reductions in $\kappa_z$ under the nanoscale hotspot compared to the uniform heating mode are 35.52, 25.76, 19.98, and 14.08 W·m$^{-1}$·K$^{-1}$. At temperatures of 300 K and 600 K, the maximum values of the anomalous enhancement are 7.99 and 5.57 W·m$^{-1}$·K$^{-1}$, respectively. The calculation results exhibit some oscillation; however, as the temperature increases, the maximum values of the anomalous enhancement show a decreasing trend. The enhanced phonon anharmonic scattering at elevated temperatures [60] significantly reduces the phonon MFP in silicon [61], thereby altering its nonequilibrium transport mode. Our results further demonstrate that the nonequilibrium phonon effect around nanoscale hot spots is progressively suppressed as the temperature rises. Spectral $\kappa_z$ at different temperatures near the hotspot and at the anomalous enhancement position are provided in the Appendix G of SM.

Finally, we systematically investigated the dependence of the total thermal resistance of the system on the heat source size, as presented in Fig. 8. As the $L_{hot}$ decreases, the thermal resistance at both the heat source and the system regions increases significantly. Among them, the increase in thermal resistance at the heat source is more pronounced than that within the system. When $L_{hot}$ =10.9 nm, the increase reaches its maximum, the thermal resistance at the heat source and the system are 6.4 times and 2.5 times those under uniform heating, respectively. In contrast, the size of the nanoscale heat source has a negligible effect on the thermal resistance at the heat sink. Overall, in contrast to the preceding analysis of $\kappa_z(\omega)$ and cumulative $\kappa_z$ at specific positions, in this part we provide a more holistic description of the suppressed thermal transport properties of the system under the influence of nanoscale hotspot.

In this study, we employed NEMD simulation to systematically investigate the thermal conduction characteristics of bulk silicon at room temperature under excitation by nanoscale hotspot with sizes ranging from 10 to 41 nm. We reported the spatially anomalous distribution of thermal conductivity induced by nanoscale heat sources, the thermal conductivity in the region adjacent to the heat source decreases by up to 68%, while a local anomalous enhancement of approximately 12% is observed in specific areas. Spectral analysis indicates that the nonequilibrium effects arising from the nanoscale hotspot markedly suppress the phonon thermal conduction in regions near the nanoscale hotspot, with the suppression being particularly pronounced for low-frequency phonons. This suppression gradually weakens as heat transport distance increases. At a distance of approximately 40 nm from the heat source, the spectral thermal conductivity approaches or even slightly exceeds that observed under uniform heating conditions. The study suggests that the non-Fourier heat conduction induced by the nanoscale heat source, along with its restructuring effect on phonon transport mechanisms, constitutes the core cause of the observed phenomena. These findings provide direct computational evidence for understanding the unique characteristics of thermal transport in nanoscale systems.

## Conflict of Interest

The authors have no conflicts to disclose.

## Author Contributions

Yuxin Luo: Data curation (lead); Formal analysis (equal); Investigation (lead); Methodology (equal); Software (lead); Visualization (lead); Writing – original draft (lead); Writing – review & editing (equal). Shuai Wu: Data curation (equal); Formal analysis (equal); Investigation (equal); Visualization (equal); Software (equal); Dongdong Kang: Methodology (equal); Supervision (equal); Validation (equal); Writing – review & editing (equal). Xiaoxiang Yu: Conceptualization (equal); Data curation (equal); Formal analysis (equal); Investigation (equal); Methodology (lead); Project administration (equal); Resources (equal); Software (equal); Supervision (lead); Validation (lead); Visualization (equal); Writing – original draft (lead); Writing – review & editing (equal). Jiayu Dai: Conceptualization (equal); Data curation (equal); Formal analysis (equal); Funding acquisition (lead); Investigation (equal); Methodology (equal); Project administration (lead); Resources (equal); Software (equal); Supervision (lead); Validation (equal); Visualization (equal); Writing – original draft (equal); Writing – review & editing (equal).

## Data availability

The data that support the findings of this study are available from the corresponding authors upon reasonable request.

## Acknowledgments

This work was supported by the National Natural Science Foundation of China (Grant Nos. 12534013 and 12304307), the Innovation Research Foundation of National University of Defense Technology, and the Science and Technology Innovation Program of Hunan Province (Grant Nos. 2025ZYJ001 and 2021RC4026).

## References


[1] Lv H, Jing D, and Zhan W 2021 *J. Phys. : Conf. Ser.* **2033** 012138
[2] Yan Z, Liu G, Khan J M, and Balandin A A 2012 *Nat. Commun.* **3** 827
[3] Huang X, Ma S, Zhao C Y, Wang H, and Ju S 2023 *npj Comput. Mater.* **9** 191
[4] Rao Y, Zhao C Y, Shen L, and Ju S 2023 *Phys. Rev. B* **108** 085413
[5] Jeong W, Kim K, Kim Y, Lee W, and Reddy P 2014 *Sci. Rep.* **4** 4975
[6] Martinez A, Barker J R, Aldegunde M, and Valin R 2015 *IEEE Electron Device Lett.* **36** 2
[7] Cometto O, Samani M K, Liu B, Sun S, Tsang S H, Liu J, Zhou K, and Teo E H T 2017 *ACS Appl. Mater. Interfaces* **9** 7456
[8] Choi D, Poudel N, Park S, Akinwande D, Cronin S B, Watanabe K, Taniguchi T, Yao Z, and Shi L 2018 *ACS Appl. Mater. Interfaces* **10** 11101
[9] Hu B, Wang Z, Xu K, and Tang D 2025 *Int. J. Heat Mass Transf.* **241** 126679
[10] Zhang H, Wang H, Xiong S, Han H, Volz S, and Ni Y 2018 *J. Phys. Chem. C* **122** 2641
[11] Dionne C J, Thakur S, Scholz N, Hopkins P, and Giri A 2024 *npj Comput. Mater.* **10** 177
[12] Liu F and Gao P 2025 *Chin. Phys. Lett.* **42** 080713
[13] Feng S, Chen H, Zhang J, An M, and Zhang G 2026 *Chin. Phys. Lett.* **43** 020801
[14] Yue J, Chen R, Ma D, and Hu S 2025 *Chin. Phys. Lett.* **42** 036301
[15] Cahill D G, Braun P V, Chen G, Clarke D R, Fan S, Goodson K E, Keblinski P, King W P, Mahan G D, Majumdar A, Maris H J, Phillpot S R, Pop E, and Shi L 2014 *Appl. Phys. Rev.* **1** 011305
[16] Chen G 2021 *Nat Rev Phys* **3** 555
[17] Regner K T, Sellan D P, Su Z, Amon C H, McGaughey A J H, and Malen J A 2013 *Nat. Commun.* **4** 1640
[18] Li H, Zhang E, Duan S, Wu S, Zhong L, Chen H, Li Y, Kang D, Chen B, Yu X, and Dai J 2025 *Appl. Phys. Rev.* **127** 132202
[19] Xu J, Hu Y, and Bao H 2023 *Phys. Rev. Applied* **19** 014007
[20] Zhang C, Ma D, Shang M, Wan X, Lü J T, Guo Z, Li B, and Yang N 2022 *Mater. Today Phys.* **22** 100605
[21] Huang D, Sun Q, Liu Z, Xu S, Yang R, and Yue Y 2023 *Adv. Sci.* **10** 2204777
[22] Xu J, Huang X, Sheng Y, Sun Q, Zhang H, Bao H, and Yue Y 2025 *Adv. Sci.* **12** 2411040
[23] Sullivan S, Vallabhaneni A, Kholmanov I, Ruan X, Murthy J, and Shi L 2017 *Nano Lett.* **17** 2049
[24] Zeng L and Chen G 2014 *J. Appl. Phys.* **116** 064307
[25] Sverdrup P G, Sinha S, Asheghi M, Uma S, and Goodson K E 2001 *Appl. Phys. Lett.* **78** 3331
[26] Chen X, Hua C, Zhang H, Ravichandran N K, and Minnich A J 2018 *Phys. Rev. Applied* **10** 054068
[27] Zeng L, Collins K C, Hu Y, Luckyanova M N, Maznev A A, Huberman S, Chiloyan V, Zhou J, Huang X, Nelson K A, and Chen G 2015 *Sci. Rep.* **5** 17131
[28] Luo T and Chen G 2013 *Phys. Chem. Chem. Phys.* **15** 3389
[29] Sheng Y, Hu Y, Fan Z, and Bao H 2022 *Phys. Rev. B* **105** 075301
[30] Sellan D P, Landry E S, Turney J E, McGaughey A J H, and Amon C H 2010 *Phys. Rev. B* **81** 214305
[31] Zhang E, Yao Y, Gao T, Kang D, Wu J, and Dai J 2019 *J. Chem. Phys.* **151** 064116
[32] Huberman S, Chiloyan V, Duncan R A, Zeng L, Jia R, Maznev A A, Fitzgerald E A, Nelson K A, and Chen G 2017 *Phys. Rev. Materials* **1** 054601
[33] Anufriev R, Gluchko S, Volz S, and Nomura M 2018 *ACS Nano* **12** 11928
[34] Zhang W, Xiong S, Guo Y, Yi H L, Nomura M, and Volz S 2025 *ACS Nano* **19** 37004
[35] Ding W, Shiomi J, and Cao B 2026 *Chinese Phys. Lett.* **43** 040801
[36] Hu Y, Zeng L, Minnich A J, Dresselhaus M S, and Chen G 2015 *Nat. Nanotechnol.* **10** 701
[37] Siemens M E, Li Q, Yang R, Nelson K A, Anderson E H, Murnane M M, and Kapteyn H C 2010 *Nat. Mater.* **9** 26
[38] Minnich A J, Johnson J A, Schmidt A J, Esfarjani K, Dresselhaus M S, Nelson K A, and Chen G 2011 *Phys. Rev. Lett.* **107** 095901
[39] Koh Y K and Cahill D G 2007 *Phys. Rev. B* **76** 075207
[40] Yue Y, Chen X, and Wang X 2011 *ACS Nano* **5** 4466
[41] Habibi M, Beardo A, and Cui L 2025 *ACS Nano* **19** 6033
[42] Pan D, Li T, Wan X, Zong Z, Qin Y, and Yang N 2025 *Chin. Phys. Lett.* **42** 070801
[43] Chang X, Kang D, Chen B, and Dai J 2025 *Chin. Phys. Lett.* **42** 053704
[44] Chen K, Chen B, Cui Y, Yu Y, Yu J, Geng H, Kang D, Wu J, Shen Y, and Dai J 2024 *Matter Radiat. Extremes* **9** 027802
[45] Chen B, Zeng Q, Yu X, Chen J, Zhang S, Kang D, and Dai J 2026 *Matter Radiat. Extremes* **11** 017603
[46] Fan Z, Siro T, and Harju A 2013 *Comput. Phys. Commun.* **184** 1414
[47] Maiti A, Mahan G D, and Pantelides S T 1997 *Solid State Commun.* **102** 517
[48] Qiu R, Zeng Q, Chen B, Han J, Chen J, Tong Q, Chen K, Kang D, Yu X, Wang H, and Dai J 2026 *Phys. Rev. Lett.* **136** 016301
[49] Xiao H, Yu X, Qiu R, Wu S, Chang X, Zeng Q, Deng C, Zhang T, Kang D, and Dai J 2026 *J. Chem. Phys.* **164** 184504
[50] Zeng Q, Yu X, Chen B, Zhang S, Chen K, Kang D, and Dai J 2025 *Nat. Commun.* **16** 10464
[51] Chang X, Chen B, Zeng Q, Wang H, Chen K, Tong Q, Yu X, Kang D, Zhang S, Guo F, Hou Y, Zhao Z, Yao Y, Ma Y, and Dai J 2024 *Nat. Commun.* **15** 8543
[52] Qiu R, Zeng Q, Han J, Chen K, Kang D, Yu X, and Dai J 2025 *Phys. Rev. B* **111** 064103
[53] Wu S, Kang D, Yu X, and Dai J 2024 *Appl. Phys. Lett.* **125** 142206
[54] Fan Z, Wang Y, Gu X, Qian P, Su Y, and Ala-Nissila T 2020 *J. Phys. : Condens. Matter* **32** 135901
[55] Tersoff J 1989 *Phys. Rev. B* **39** 5566
[56] Tersoff J 1988 *Phys. Rev. B* **37** 6991
[57] Fan Z, Dong H, Harju A, and Ala-Nissila T 2019 *Phys. Rev. B* **99** 064308
[58] Hu Y, Feng T, Gu X, Fan Z, Wang X, Lundstrom M, Shrestha S S, and Bao H 2020 *Phys. Rev. B* **101** 155308
[59] Feng T, Yao W, Wang Z, Shi J, Li C, Cao B, and Ruan X 2017 *Phys. Rev. B* **95** 195202
[60] Jin J S 2024 *J. Appl. Phys.* **135** 045103
[61] Maldovan M 2011 *J. Appl. Phys.* **110** 034308